Classical interpretation of probability oscillations in low-energy atomic collisions

P. Botheron and B. Pons

CELIA, Université de Bordeaux I, CNRS, CEA, 351 Cours de la Libération, F-33405 Talence, France

(Received 22 February 2011; published 15 June 2011)

We perform close-coupling molecular and classical trajectory Monte Carlo (CTMC) calculations of charge-exchange probabilities in low-energy H^+, $He^{2+} + H$ collisions. We consider head-on collisions with a zero impact parameter and study the dependence of the charge-exchange probability on the impact velocity. This probability exhibits oscillations generally understood as signatures of quantum phase effects. CTMC calculations with dimensionality reduced to one fairly reproduce the oscillations and show that these latter stem from the back and forth motion of the electron between the nuclear centers in the internuclear region. In three dimensions, the probability oscillations are generally washed out in the statistical CTMC framework because of the electron transverse degrees of freedom. However three-dimensional Bohmian trajectories ascertain the classical interpretation of the oscillations in a quantum framework.

DOI: 10.1103/PhysRevA.83.062704 PACS number(s): 34.10.+x, 34.70.+e

I. INTRODUCTION

Charge exchange in atomic collisions is quite an old topic but still motivates a considerable amount of work because of its interest in spectroscopic diagnostics of Tokamak fusion plasmas [1], interstellar medium [2], and radiation damage applications [3]. From a theoretical point of view, charge exchange is an interesting problem which underlies the description of time-dependent electron dynamics in the field of moving target and projectile centers. Depending on the perturbation strength Z_P/v, where Z_P is the (effective) projectile charge and v the impact velocity, various methods have been developed to describe the electron transfer process [4]. In the high-impact velocity range characterized by $Z_P/v > 1$, sophisticated perturbative treatments using continuum distorted waves (CDW, [5]) provide an accurate modeling of the process. In low-energy collisions where v is typically lower than the orbital velocity v_e of the electron in its initial state, the perturbative schemes do not apply and one generally implements variational schemes which consist of expanding the total electron wave function onto molecular [6,7] or atomic [8] states associated with the main scattering channels. The theoretical description becomes especially difficult in the intermediate-energy range where all the inelastic processes (charge exchange, excitation, and ionization) are of similar magnitude and must be treated on the same footing. However, continuous advances in computer performance have allowed the previous close-coupling treatments to be optimized [9,10] and new ones to be developed [11,12]; concurrently, the direct resolution of the time-dependent Schrödinger equation has became possible [13,14] so that charge exchange can nowadays be fairly described from low to high v's, at least for effective one-electron ion-atom systems.

Despite all these sophisticated descriptions, our understanding of the electron-capture process mostly rests on a classical picture in which the electron can jump from the target to the projectile at small enough internuclear distances R so that the height of the internuclear barrier, formed by the superposition of target and projectile potentials, is lower than the energy of the electron in its initial state [15]. This interpretation has been strengthened by the classical trajectory Monte Carlo (CTMC, [16]) approach which has provided total and differential cross sections in close agreement with experiment over a broad range of impact energies and collisional systems (see, e.g., Refs. [17–19]). Nevertheless the reliability of the classical picture and related CTMC calculations depends on v. In the low-impact energy range, the classical description is expected to fail both qualitatively and quantitatively.

It is indeed well known that in addition to overbarrier transitions, electron capture can also occur at low v in terms of tunneling (underbarrier) transitions at large R [4]. However, and contrarily to what may be thought at first sight, such classically forbidden transitions can be mimicked, to some extent, by means of improved CTMC calculations. These calculations employ initial conditions beyond the usual microcanonical framework [20–25] and describe the quantum electronic density by means of an improved phase-space distribution akin to, e.g., the well-known Wigner one [26,27]. Such distributions have a classical energy spread which allows one to relate the tunnel effect to the presence in the ensemble of classical states of trajectories with energies locally lying above the barrier [28,29]. Accordingly improved CTMC calculations have yielded satisfactory quantitative results for $v < v_e$, typically down to 0.5 v_e [18,19,21,30,31]. The existence of tunneling transitions thus do not appear as the main limitation of the classical description of the charge-exchange process as far as the initial quantum state is adequately represented within the statistical framework.

On the other hand, further quantum effects are expected to significantly influence the charge-exchange process at low v. As a matter of fact, the charge-exchange probability then exhibits an oscillatory behavior either as a function of the impact parameter b for fixed v or as a function of v for fixed b [4,32,33]. These oscillations are generally related to the dependence on v and b of the phase accumulated by the collisional system along the nuclear path $R(t)$ [4], and are known as Stueckelberg oscillations in relation to the pioneering work of Stueckelberg [34], who derived around 1930 an approximate semiclassical phase-integral method for the two-state scattering problem. In other words, the oscillations of probability are commonly related to interference effects between the main capture and the elastic scattering channels.

Interestingly, oscillations in total capture cross sections have been observed for singly charged ions impinging on

Rydberg atoms [35]. These oscillations have been related to the number of swaps the electron experiences between the target and the projectile centers during the collision. Schultz, Reinhold, and Krstić [36] later demonstrated that this classical phenomenom also induces oscillations in a wide range of reaction cross sections for collisions of multiply charged ions with ground-state atoms. The same authors then undertook a quantum-mechanical analysis [37], in terms of a close-coupling molecular description derived from the hidden crossings theory [6], to show that the oscillations originate from the interference of two collisional paths, namely, $|\chi_i\rangle \rightarrow |\chi_1\rangle \rightarrow |\chi_f\rangle$ and $|\chi_i\rangle \rightarrow |\chi_2\rangle \rightarrow |\chi_f\rangle$, through which the initial state $|\chi_i\rangle$ is promoted to the same final one $|\chi_f>$ (see also Ref. [38]). The dominant phase causing the interference pattern is accumulated in the incoming phase of the collision, owing to the long-range (radial) coupling of $|\chi_i\rangle$ and $|\chi_1\rangle$ and associated with the classical swapping of the electron between the nuclear centers. The incoming interference pattern remains imprinted in the cross section associated with the $|\chi_f\rangle$ channel, despite the integration on impact parameters, provided the transitions $|\chi_1\rangle \rightarrow |\chi_f\rangle$ and $|\chi_i\rangle \rightarrow |\chi_2\rangle$ occur in a narrow range of (small) internuclear distances (while $|\chi_2\rangle \rightarrow |\chi_f\rangle$ occurs in the receding stage of the collision).

In this paper, we aim to show that Stueckelberg oscillations can also be interpreted in terms of swaps of the electron between the target and the projectile nuclear centers. We even consider resonant charge-exchange processes, inherent in homonuclear systems, in which dynamics cannot be related to transitions at definite internuclear distances. Explicitly, we consider the prototypical $H^+ + H(1s)$ and $He^{2+} + H(1s)$ systems. We restrict our calculations to head-on collisions with $b = 0$ and study the dependence of the charge-exchange probability on E. As we artificially reduce the dimensionality of the collisional problems to one dimension, we unexpectedly find that CTMC calculations fairly reproduce the oscillatory behavior of the probability at low v. We pragmatically conclude that the usual interpretation, in terms of quantum-phase effects, has a classical counterpart. The CTMC electron trajectories indicate that the probability oscillations stem from the simple (and intuitive) back and forth motion of the electron between the target and the projectile centers in the molecular region. As we restore the full dimensionality of electron motion (to three dimensions), we observe that the oscillatory behavior of the probabilities is washed out in the classical calculations because the additional (transverse) degrees of freedom put the independent electron trajectories out of phase in the internuclear direction. However, picturing the charge-exchange dynamics in terms of three-dimensional (entangled) Bohmian trajectories helps to ascertain the classical interpretation of the probability oscillations.

The paper is organized as follows: In Sec. II, we outline the classical and semiclassical descriptions of one-dimensional (1D) ion-atom collisions. We report our findings in Sec. III which also contains three-dimensional (3D) illustrations of the collision dynamics. We give our conclusions in Sec. IV. Atomic units are used throughout, unless otherwise stated.

II. METHODS

We employ the impact parameter approximation [4] in which the projectile follows straight-line trajectories with constant velocity v and impact parameter b so that $\mathbf{R}(t) = \mathbf{b} + \mathbf{v}t$. This approximation is accurate for impact energies E greater than ~250 eV/amu [33,39]; however, we apply it whatever E is since we are interested in the comparison of the classical and quantum electron probabilities and not in the accuracy of the probabilities owing to nuclear motion effects. In the 1D model calculations, $b = 0$.

A. Quantum description of the electron motion in 1D model collisions

The electron motion is quantum mechanically described by the total wave function $\Psi(x,t)$, which is the solution of the eikonal equation

$$i\frac{\partial\Psi(x,t)}{\partial t} = H\Psi(x,t), \tag{1}$$

where x is the electron coordinate defined with respect to an origin located on the internuclear axis ($\hat{\mathbf{R}} = \hat{\mathbf{x}}$) at distances pR and qR from the target and projectile centers, respectively ($0 \leqslant p \leqslant 1$ and $p + q = 1$). In one-electron systems with target and projectile nuclear charges Z_T and Z_P, the clamped nuclei (Born-Oppenheimer) Hamiltonian H is

$$H = \frac{p^2}{2} - \frac{Z_T}{\sqrt{(x+pR)^2+\alpha_T^2}} - \frac{Z_P}{\sqrt{(x-qR)^2+\alpha_P^2}}, \tag{2}$$

including the kinetic energy term $p^2/2$ and the electron-target and electron-projectile interaction potentials, which are softened by means of the parameters $\alpha_{T,P} = \sqrt{2}/Z_{T,P}$ to remove Coulomb singularities on the nuclear centers.

The eikonal equation (1) has to be solved subjected to the initial condition $\Psi(x, t \rightarrow -\infty) = \phi_1^{(T)}(x)D_T(v;x,t)e^{-i\epsilon_1^{(T)}t}|_{t\rightarrow-\infty}$, where $\phi_1^{(T)}(x)$ is the initial atomic target state of energy $\epsilon_1^{(T)}$ and $D_T(v;x,t) = e^{-ipvx-ip^2v^2t}$ is the plane-wave factor which represents the drag velocity impulsed by the moving target on the electron. The eikonal equation has been solved by means of a Eulerian lattice technique employing the Crank-Nicholson scheme [40]. We have also employed a molecular close-coupling technique which consists of expanding $\Psi(x,t)$ on the eigenstates $\chi_k(x,R)$ of H according to

$$\Psi(x,t) = \sum_{k=1}^{N} a_k(v;t)\chi_k(x,R)e^{-i\int^t E_k(t')dt'}, \tag{3}$$

where $H\chi_k(x,R) = E_k(R)\chi_k(x,R)$. Inserting Eq. (3) in Eq. (1) yields the set of differential equations for the expansion amplitudes $a_k(v;t)$:

$$\frac{\partial a_l(v;t)}{\partial t} = \sum_{k=1}^{N} a_k(v;t)v\ \mathrm{sgn}(t)\left\langle \chi_l \left| \frac{\partial}{\partial R} \right| \chi_k \right\rangle \times e^{-i\int^t [E_k(t')-E_l(t')]dt'}, \tag{4}$$

where $\mathrm{sgn}(t) = -1$ when $t < 0$ and $+1$ otherwise. Care must be taken in relation with the fact that the eikonal equation is defined in the laboratory-fixed frame of reference whereas the χ states are defined in the molecular frame. Passing through the united-atom limit at $t = 0$, the molecular frame experiences

a sudden rotation of π with respect to the fixed frame. In the united-atom limit, the one-dimensional χ states transform into atomic states of given (odd or even) symmetry; this means that $\chi_m(x,t=0^+) = -\chi_m(-x,t=0^-)$ if m is even (the minimum value of m is 1) while $\chi_m(x,t=0^+) = \chi_m(-x,t=0^-)$ if is m is odd. We account for this consequence of the sudden rotation of the molecular frame in Eq. (4) by changing the sign of the amplitudes associated with odd states as $t=0$ is crossed.

For each impact velocity v, the system (4) is numerically integrated from $t_{\rm in} = -50/v$, where

$$a_k(v;t_{\rm in}) = \left\langle \chi_k e^{-i\int^{t_{in}} E_k(t')dt'} \middle| \phi_1^{(T)} D_T(t_{\rm in}) e^{-i\epsilon_1^{(T)} t_{\rm in}} \right\rangle \tag{5}$$

to $t_{\rm max} = 100/v$, where the capture probabilities into the $\phi_m^{(P)}$ bound atomic projectile states are computed as

$$P_{C,m}(v) = \left| \sum_{k=1}^{N} a_k(v;t_{\rm max}) \left\langle \phi_m^{(P)} D_P(t_{\rm max}) \middle| \chi_k e^{-i\int^{t_{\rm max}} E_k(t')dt'} \right\rangle \right|^2, \tag{6}$$

where $D_P(t) \equiv D_P(v;x,t) = e^{iqvx - iq^2v^2t}$, while for excitation

$$P_{E,m}(v) = \left| \sum_{k=1}^{N} a_k(v;t_{\rm max}) \left\langle \phi_m^{(T)} D_T(t_{\rm max}) \middle| \chi_k e^{-i\int^{t_{\rm max}} E_k(t')dt'} \right\rangle \right|^2. \tag{7}$$

Assuming that the target and projectile atomic basis are not overcomplete at $t_{\rm max}$, we use closure relations to finally define the ionization probability $P_{\rm ion}(v) = 1 - \sum_m P_{C,m}(v) - \sum_{m'} P_{E,m'}(v)$.

As explained in Ref. [25], the atomic states $\{\phi_m^{(T,P)}\}$ are obtained by diagonalizing the target (projectile) Hamiltonian in a basis of $\cos(kx)$ and $\sin(kx)$ functions confined in a box of length $2x_{\rm max}^{(T,P)}$ centered on the target (projectile) nucleus. In practice, the underlying basis contains all the $\cos(kx)$ and $\sin(kx)$ functions such that $\cos(kx_{\rm max}^{(T,P)}) = 0$ and $\sin(kx_{\rm max}^{(T,P)}) = 0$, respectively, with $0 \leqslant k \leqslant k_{\rm max}^{(T,P)}$. Similarly, the molecular wave functions $\{\phi_m(x,R)\}$ are obtained by diagonalizing the total Hamiltonian H of Eq. (2) for fixed R's in a basis of confined $\cos(kx)$ and $\sin(kx)$ functions. In this case, the box of length $2x_{\rm max}$ is centered on the origin of electronic coordinates and the momentum scale is restricted to $k \leqslant k_{\rm max}$. The latter diagonalization yields a huge number of $\chi_m(x,R)$ eigenstates, including discretized continuum ones. In the framework of molecular close-coupling approaches, one has to check the sign consistency of the diagonalized molecular eigenstates as R varies from 0 to $vt_{\rm max}$ [41] in order to manipulate well-behaved radial couplings in Eq. (4) throughout the collision. To cope with the fact that diagonalization yields eigenstates with random signs at each R, we proceed as follows: we define an x grid of dimension $\mathcal{N}$ within which we only retain the $\mathcal{N}_{\rm ret}$ points x_k such that $\chi_m(x_k,R) > S$ and $\chi_m(x_k,R+\Delta R) > S$, with S typically of the order of 10^{-2}; for these $\mathcal{N}_{\rm ret}$ points we calculate

$$\begin{aligned} |\chi_m(x_k,R) - \chi_m(x_k,R+\Delta R)| &= D^-, \\ |\chi_m(x_k,R) + \chi_m(x_k,R+\Delta R)| &= D^+. \end{aligned} \tag{8}$$

If the number of grid points such that $D^- < D^+$ is larger than that for which $D^- > D^+$, the sign is declared to be consistent between R and $R+\Delta R$; if the reverse occurs, the sign of χ_m is changed at $R+\Delta R$. This procedure is reliable even for the discretized continuum states.

Concerning the computation of the radial couplings entering Eq. (4), we circumvent the derivation with respect to R of the diagonalization coefficients $c_p^l(R)$ resulting from the diagonalization of H following [42]

$$\left\langle \chi_l \middle| \frac{\partial}{\partial R} \middle| \chi_k \right\rangle = \frac{1}{E_k - E_l} \sum_{p,q} c_p^l(R) c_q^k(R) \frac{\partial}{\partial R} \langle \psi_p | H | \psi_q \rangle, \tag{9}$$

where the $\{\psi_q\}$ stand for the underlying $\cos(k_q x)$ and $\sin(k_q x)$ functions. Since ψ_q does not depend on R, we finally obtain

$$\left\langle \chi_l \middle| \frac{\partial}{\partial R} \middle| \chi_k \right\rangle = \frac{1}{E_k - E_l} \left\langle \chi_l \middle| \frac{\partial H}{\partial R} \middle| \chi_k \right\rangle, \tag{10}$$

which is easily computed using $\partial H/\partial R = Z_T p(x+pR)[(x+pR)^2+\alpha_T^2]^{-3/2} - Z_P q(x-qR)[(x-qR)^2+\alpha_P^2]^{-3/2}$.

The case of homonuclear systems, with $Z_P = Z_T$, deserves special attention. In such systems, the main charge-exchange channel is symmetrically resonant with the elastic scattering one so that a two-state molecular expansion, including only these channels, is generally sufficient to account for the whole capture process at low v [4]. If the origin of electronic coordinates is chosen at the geometrical center of the system ($p = 1/2$), the radial coupling linking these two channels vanishes since they present *gerade* and *ungerade* symmetries, respectively. If we label χ_1 and χ_2 the respective *gerade* and *ungerade* molecular states, we thus have according to Eq. (4), and taking into account the sudden rotation of the molecular frame at $t=0$, $a_1(v;+\infty) = a_1(v;-\infty)$ and $a_2(v;+\infty) = -a_2(v;-\infty)$. The initial target state $\phi_1^{(T)}$ corresponds to $\lim_{R\to\infty}[\chi_1(x,R) + \chi_2(x,R)]/\sqrt{2}$ while the resonant capture state $\phi_1^{(P)}$ is $\lim_{R\to\infty}[\chi_1(x,R) - \chi_2(x,R)]/\sqrt{2}$. Neglecting the plane-wave factor in the definition of the initial and final conditions (5) and (6), which is justified at (very) low velocities [43], we finally obtain $a_1(v;+\infty) = -a_2(v;+\infty) = 1/\sqrt{2}$ so that the capture probability is

$$P_{C,1}(v) = \cos^2 \frac{1}{v} \int_0^\infty [E_2(R) - E_1(R)] dR. \tag{11}$$

The probability oscillates with unit amplitude as a function of v. The oscillations are monitored by the phase difference between the lowest gerade and ungerade pathways, which should not be at first sight reproducible in terms of classical mechanics. However, we shall illustrate hereinafter that the quantum-mechanical interpretation has a classical analog in terms of the behavior of classes of trajectories.

B. CTMC description of the electron motion in 1D model collisions

In our classical description of the electron dynamics, the origin of electronic coordinates is placed on the target nucleus ($p = 0$). The statistical CTMC procedure [16] employs an

N-point discrete representation of the phase-space distribution $\varrho(x,p,t)$,

$$\varrho(x,p,t) = \frac{1}{N}\sum_{j=1}^{N}\delta(x - x_j(t))\delta(p - p_j(t)), \tag{12}$$

which transforms the Liouville equation [the classical analog to the eikonal equation (1)],

$$\frac{\partial\varrho(x,p,t)}{\partial t} = -[\varrho(x,p,t),H], \tag{13}$$

where $[\varrho(x,p,t),H]$ is the Poisson bracket, into the well-known Hamilton equations

$$\begin{aligned}\frac{\partial x_j(t)}{\partial t} &= p_j(t),\\ \frac{\partial p_j(t)}{\partial t} &= -\frac{Z_T x_j(t)}{\left[x_j(t)^2+\alpha_T^2\right]^{3/2}} - \frac{Z_P(x_j(t)-R(t))}{\left\{[x_j(t)-R(t)]^2+\alpha_P^2\right\}^{3/2}},\end{aligned} \tag{14}$$

which monitor the temporal evolution of the jth electronic trajectory among the set of N noninteracting ones.

In the present work, we mainly use an initial microcanonical phase-space distribution,

$$\begin{aligned}\varrho(x,p,t_{\rm in}) &= \varrho_M\left(\epsilon_1^{(T)};x,p\right)\\ &= \kappa\delta\left(\frac{p^2}{2} - \frac{Z_T}{\sqrt{x^2+\alpha_T^2}} - \epsilon_1^{(T)}\right),\end{aligned} \tag{15}$$

which assigns the energy $\epsilon_1^{(T)}$ of the quantum initial state to the energy of all the N electrons at time $t = t_{\rm in}$. κ is a normalization constant so that $\int\int\varrho(x,p,t_{\rm in})dxdp = 1$. The construction and characteristics of the microcanonical $\varrho(x,p,t_{in})$ associated with the 1D H($n = 1$) are detailed in Ref. [25]. In the same reference, we explain how to build an initial distribution that better reproduces the quantum electron densities in terms of the truncated Wigner distribution:

$$\begin{aligned}\varrho(x,p,t_{\rm in}) &= \varrho_{Wt}(x,p)\\ &= \int_{\epsilon_{\rm min}^{(T)}}^{\epsilon_1^{(T)+}} f_W(\epsilon^{(T)})\varrho_M(\epsilon^{(T)};x,p)d\epsilon^{(T)}.\end{aligned} \tag{16}$$

$\varrho_M(\epsilon^{(T)};x,p)$ is a microcanonical distribution of energy $\epsilon^{(T)}$ [see Eq. (15)] and

$$\begin{aligned}f_W(\epsilon^{(T)}) &= \frac{1}{N_W}\int\varrho_W(x,p)\\ &\quad\times\delta\left(\frac{p^2}{2} - \frac{Z_T}{\sqrt{x^2+\alpha_T^2}} - \epsilon_1^{(T)}\right)dxdp\end{aligned} \tag{17}$$

is the classical energy distribution associated with the Wigner distribution $\varrho_W(x,p)$ of the initial quantum state $\phi_1^{(T)}(x)$. In Eq. (16), $f_W(\epsilon^{(T)})$ is truncated to $[\epsilon_{\rm min}^{(T)},\epsilon_1^{(T)+}]$, where $\epsilon^{(T)+}$ is the upper bound of the classical energy bin associated with the initial $\phi_1^{(T)}$ state, and $\epsilon_{\rm min}^{(T)}$ and N_W are introduced so that $\int_{\epsilon_{\rm min}^{(T)}}^{\epsilon_1^{(T)+}} f_W(\epsilon^{(T)})d\epsilon^{(T)} = 1$ and $\int_{\epsilon_{\rm min}^{(T)}}^{\epsilon_1^{(T)+}} f_W(\epsilon^{(T)})\epsilon^{(T)}d\epsilon^{(T)} = \epsilon_1^{(T)}$.

Once the trajectories have been propagated up to $t = t_{\rm max}$, we discriminate between the various inelastic processes using energy criteria: a trajectory is ascribed to capture if its energy with respect to the target, $\epsilon_j^{(T)}(t_{\rm max}) = p_j^2(t_{\rm max})/2 - Z_T/\sqrt{x_j(t_{\rm max})^2+\alpha_T^2}$, is positive and its energy with respect to the projectile, $\epsilon_j^{(P)}(t_{\rm max}) = [p_j(t_{\rm max}) - v]^2/2 - Z_P/\sqrt{[x_j(t_{\rm max})-R]^2+\alpha_T^2}$, is negative; a trajectory belonging to excitation (including elastic scattering) fulfills $\epsilon_j^{(T)}(t_{\rm max}) < 0$ and $\epsilon_j^{(P)}(t_{\rm max}) > 0$, while for ionization, $\epsilon_j^{(T,P)}(t_{\rm max}) > 0$. The probabilities for capture $P_C^{\rm clas}$, excitation $P_E^{\rm clas}$, and ionization $P_I^{\rm clas}$ are then defined by counting, among the N electrons, those who obey the previous criteria, respectively,

$$P_{C,E,I}^{\rm clas}(v) = \frac{N_{C,E,I}}{N}. \tag{18}$$

State-selective excitation and capture probabilities can be computed after partitioning the classical negative-energy scales of the target and the projectile in order to associate energy bins $[\epsilon_n^{(T,P)-},\epsilon_n^{(T,P)+}]$ with the atomic quantum states $\phi_n^{(T,P)}$ of energy $\epsilon_n^{(T,P)}$ [25]. The partial probabilities are computed using statistical counting similar to that in Eq. (18).

C. Three-dimensional calculations and Bohmian trajectories

Three-dimensional calculations have been carried out to gauge the effect of the additional degrees of freedom with respect to the previous calculations with restricted (1D) dimensionality. The electron-target and electron-projectile potentials are no longer softened and reduce to true Coulomb potentials for one-electron systems.

The 3D CTMC calculations employ the numerical scheme originally proposed by Abrines and Percival [16]. The initial conditions are microcanonical and the calculation of total and partial probabilities is detailed in, e.g., Ref. [31].

The quantum-mechanical treatment consists of a close-coupling molecular expansion similar to that in Eq. (3) but the $\chi_k(\mathbf{r},R)$ states are one-electron-diatomic-molecule (OEDM) orbitals corrected by a common translation factor (CTF) as in Ref. [7]. The molecular expansions that have been used are restricted to bound OEDM orbitals which asymptotically correlate to capture and excitation atomic states; such expansions are far from being complete, contrarily to the previous 1D one (3), so that the CTF has to be included to fulfill the asymptotic scattering conditions and to yield Galilean-invariant probabilities [43].

Once the total wave function $\Psi(\mathbf{r},t)$ is known, one can display in the course of the collision snapshots of the electron density in both configuration and momentum spaces in order to shed light on the electron dynamics (see, for instance, Refs. [43–48]). Nonetheless, the resulting quantum pictures remain less illustrative than the classical ones that provide continuous electron trajectories, with well-defined position $\mathbf{r}(t)$ and momentum $\mathbf{p}(t)$, throughout the collision. We thus have decided to adopt the Bohmian formulation of quantum mechanics [49–51] that allows one to picture the dynamics by means of continuous quantum trajectories. The hydrodynamical (Bohm) formulation consists of likening the electron density to a fluid described in terms of N_B trajectories located, at time t, at $\mathbf{r}_j(t)$ with velocities $\mathbf{v}_j(t)$ and weights $\rho_j \equiv |\Psi(\mathbf{r}_j(t),t)|^2 (j = 1,...,N_B)$. Writing the total wave function

in its polar form, $\Psi(\mathbf{r},t) = \sqrt{\rho(\mathbf{r},t)}\exp[iS(\mathbf{r},t)]$, the velocity $\mathbf{v}_j(t)$ is defined according to

$$\frac{d\mathbf{r}}{dt}|_j = \mathbf{v}_j(t) \equiv \mathbf{v}|_j = \nabla S|_j, \tag{19}$$

which is used, together with $\partial/\partial t = d/dt - \mathbf{v}\cdot\nabla$, to derive from the eikonal equation (1) the equations

$$\left.\frac{d\rho}{dt}\right|_j = -\rho_j \nabla\cdot v|_j, \tag{20}$$

$$\left.\frac{dS}{dt}\right|_j = \frac{v_j^2}{2} - (V_T + V_P + V_Q)|j, \tag{21}$$

where V_T and T_P, respectively, stand for the classical electron-target and electron-projectile interaction potentials. It is noteworthy that Eq. (20) is the continuity equation for the electron density ρ while Eq. (21) is known as the quantum Hamilton-Jacobi (HJ) equation [51], since it includes, with respect to the classical HJ formulation, the additional term $V_Q(\mathbf{r},t) = -\nabla^2\sqrt{\rho(\mathbf{r},t)}/2\sqrt{\rho(\mathbf{r},t)}$, which is generally referred to as the quantum (Bohm) potential [51]. Equations (19)–(21) monitor the temporal evolution of the quantum trajectory j among the set of N_B ones. These equations are known to be (very) difficult to solve self-consistently since small errors in the computation of the quantum V_Q degrade the subsequent propagation of all the trajectories (see, however, Ref. [52]). Only recently some numerical procedures, mainly borrowed from plasma physics [51], have allowed us to implement self-consistently the Bohmian hydrodynamical approach, provided the dimensionality of the problem is not too high [51,53]. In the present work, we do not seek a self-consistent solution but rather aim at displaying, in the course of the collision, the temporal evolution $\mathbf{r}_j(t)$ of the quantum trajectories. We thus take advantage of the knowledge of the total wave function Ψ resulting from our CTF-modified molecular calculations to compute, on a fine 3D Eulerian grid, the velocity field $\mathbf{v}(\mathbf{r},t) = \mathbf{j}(\mathbf{r},t)/|\Psi(\mathbf{r},t)|^2$, where $\mathbf{j}(\mathbf{r},t)$ is the current density

$$j(\mathbf{r},t) = \frac{i}{2}[\Psi^*(\mathbf{r},t)\nabla\Psi(\mathbf{r},t) - \Psi(\mathbf{r},t)\nabla\Psi^*(\mathbf{r},t)]. \tag{22}$$

The Bohmian trajectories are then directly recovered by interpolation of the Eulerian velocity field $\mathbf{v}(\mathbf{r},t)$ on the Lagrangian (Bohmian) grid dictated by $\mathbf{r}_j(t) = \mathbf{r}_j(t-\Delta t) + \mathbf{v}_j(t-\Delta t)\Delta t$, with $\Delta t \sim 10^{-3}$ a.u. the small time step used in the molecular calculations. Besides user-supplied initial conditions $\mathbf{r}_j(t_{\rm in})$ $(j = 1,\ldots,N_B)$, we have $\mathbf{v}_j(t_{\rm in}) = \nabla U(\mathbf{r}_j(\mathbf{t}_{\rm in}),\mathbf{t}_{\rm in})$, where $U(\mathbf{r},t)$ is the CTF explicated in Ref. [7], which tends to $\mathbf{v}_j(t_{\rm in}) \sim -p\mathbf{v}$ in the asymptoptic ingoing phase of the collision according to the initial condition (5).

III. RESULTS

We first illustrate our findings for $H^+ + H(n=1)$ collisions where the classical description of the capture process at low v is expected to strongly fail according to Eq. (11) and then we consider $He^{2+} + H(n=1)$ collisions where phase effects also affect the probabilities according to Eqs. (4) and (6).

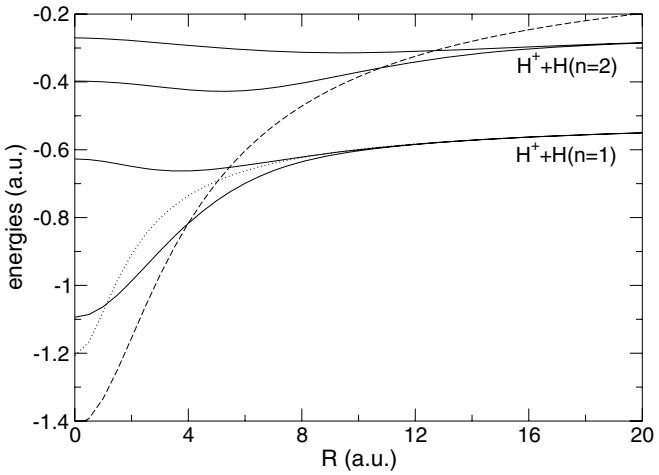

FIG. 1. Correlation diagram of the 1D $H^+ + H$ system: the plain lines correspond to the molecular energies $E_n(R)$ as functions of the internuclear distance R; the dotted line refers to the energy of the electron in its initial target state perturbed by the projectile located at distance R; and the dashed line illustrates the height of the internuclear potential barrier as a function of R.

A. $H^+ + H(n=1)$

1. One-dimensional calculations

The 1D H states are obtained by diagonalization of the atomic Hamiltonian in a $\{\cos(kx), \sin(kx)\}$ basis defined by $x_{\rm max}^{(T,P)} = 50$ a.u. and $k_{\rm max}^{(T,P)} = 3$ a.u. The diagonalized basis $\{\phi_q(x)^{(T,P)}\}$, which is identical for T and P, includes 11 bound and 83 discretized continuum states. The molecular states $\{\chi_m(x,R)\}$ are obtained similarly by diagonalizing H (2) in a basis characterized by $x_{\rm max} = 150$ a.u. and $k_{\rm max} = 3$ a.u., yielding 29 bound and 257 discretized continuum molecular wave functions. The classical CTMC calculations employ $N = 30\,000$ noninteracting trajectories.

We present in Fig. 1 the correlation diagram of the $H^+ + H$ system, emphasizing the energy region where resonant charge exchange $H^+ + H(n=1) \to H(n=1) + H^+$ occurs. To elicit the range of internuclear distances where capture transitions can occur in a pure (overbarrier) classical framework, we also include in Fig. 1 the energy of the electron in its initial target state perturbed by the projectile located at distance R, $E_{1p}(R)$, and the height $V_{\rm max}(R)$ of the internuclear barrier formed by the superposition of the electron-target and electron-projectile potentials. Assuming that the target electron is, on the average, located on the nucleus, we have $E_{1p}(R) = \epsilon_1^{(T)} - 1/\sqrt{R^2+2}$ [since $\alpha_T = \alpha_P = \sqrt{2}$ in Eq. (2)] while the internuclear potential is maximum at the geometrical center of the H_2^+ quasimolecule with $V_{\rm max}(R) = -2/\sqrt{R^2/4+2}$. Electron hops from the target to the projectile are classically allowed when $E_{1p}(R) > V_{\rm max}(R)$, i.e., for $R \leqslant R_{\rm ob} \sim 5$ a.u.

The total capture probability resulting from our molecular calculations with 286 states is displayed in Fig. 2 as a function of the impact energy E in the range $0.05 \leqslant E \leqslant 100$ keV. We explicitly show that dynamical calculations carried out with $p = 0$ and $p = 1/2$ yield the same results; this Galilean invariance, also verified at the level of partial probabilities, signifies the effective completeness of the underlying $\{\cos(kx), \sin(kx)\}$ basis in the confined $x_{\rm max}$ box. Furthermore, only the two

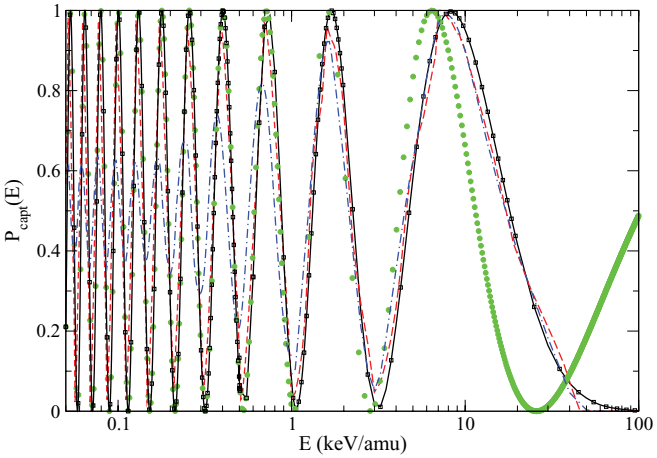

FIG. 2. (Color online) Total capture probability in 1D $H^+ + H(n = 1)$ collisions as a function of the impact energy E: large-scale molecular calculations with $p = 0$ (—) and $p = 1/2$ (□); expected results (green •) from the two-state expansion (11); and microcanonical (red dashed line) and truncated Wigner (blue dot-dashed line) CTMC calculations.

lowest molecular states among the 286 ones are necessary to obtain reliable capture probabilities at $E \leqslant 1$ keV, as can be checked in Fig. 2 by comparison of our large-scale results with the expression (11) associated with the minimal two-state expansion without translation factor.

As expected from Eq. (11), the capture probability oscillates as a function of E. Nevertheless, the quantum interpretation of the oscillations, in terms of the phase difference between the gerade and ungerade scattering channels, can certainly be linked to a classical picture since the CTMC calculations are found in Fig. 2 to be able to reproduce the oscillatory behavior of the probability. The classical results are slightly out of phase with respect to the quantum ones and the dephasing is increasing as E decreases. The origin of this minor deviation will be understood in the light of the behavior of the CTMC electron trajectories that shall elucidate the origin of the classical probability oscillations.

We have randomly sorted some CTMC electron trajectories among the $N = 30\,000$ ones to compare their temporal evolution at different impact energies within an oscillation of the total capture probability. We concentrate our attention on the oscillation enclosed in the [0.147,0.21] keV energy interval. For $E = 0.147$ keV, where $P_C^{\rm clas} \sim 0$, we display in Fig. 3(a) the evolution $x_j(t)$ of the sorted CTMC trajectories. Up to $vt \sim -5$ a.u., all the trajectories are blocked in the target potential well. Later on, they enter into the overbarrier region previously identified (in Fig. 1) to $-5 \leqslant vt \leqslant 5$ a.u.; within this time interval, the trajectories experience a back and forth motion between the target and the projectile centers as they consecutively bounce against the exterior walls of the total potential. Finally, all the trajectories localize on the target center at about $vt \sim 5$ a.u., which marks the upper bound of allowed (overbarrier) transitions. The initial dispersion of the trajectories within the target's potential well induces a delay between the subsequent dynamics of the trajectories. However this delay is small, so that a whole (average) motion clearly shows up in Fig. 3(a), because the electronic velocity v_e is

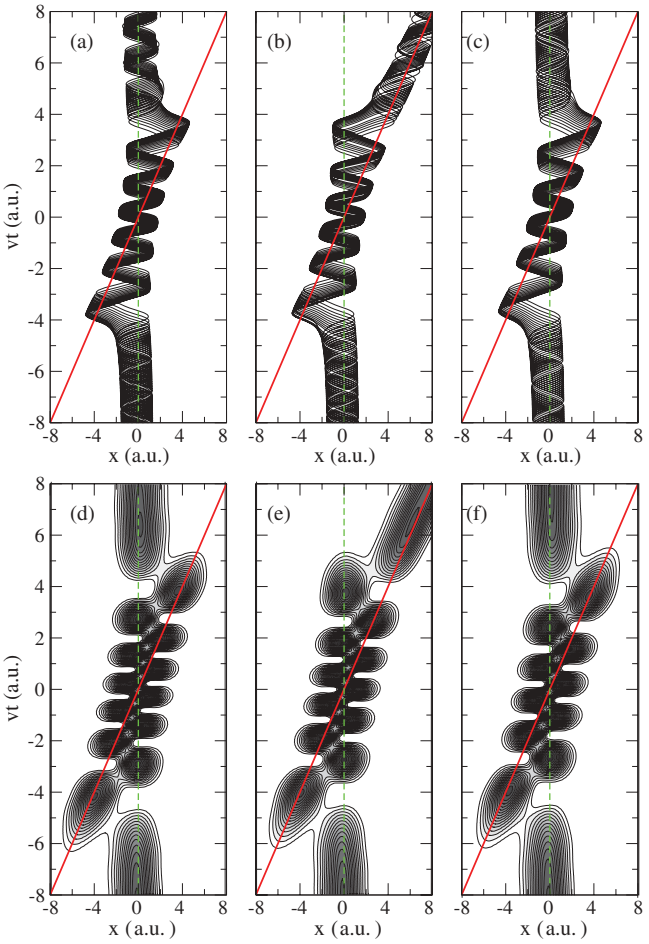

FIG. 3. (Color online) Temporal evolution $x_j(t)$ of randomly sorted CTMC electron trajectories in 1D $H^+ + H(n = 1)$ collisions (a–c). The trajectories (black thin lines) are displayed as functions of the scaled time vt for the impact energies $E = 0.147$ (a), 0.173 (b), and 0.21 (c) keV. The target (dashed green line) remains located at $x = 0$ for all t and the projectile trajectory $x(t) = vt$ is drawn with a thick (red) line. Temporal evolution of the quantum-mechanical electron density $|\Psi(x,t)|^2$ for $E = 0.147$ (d), 0.173 (e), and 0.21 (f) keV.

significantly larger than the impact one; in other words, the initial phase of the electron is not important.

In Fig. 3(b), we display the temporal evolution of the CTMC trajectories as in Fig. 3(a) but for $E = 0.173$ keV, where $P_C^{\rm clas}$ reaches its maximal value ∼1 (see Fig. 2). Once again, the trajectories are subjected to a back and forth motion between the target and projectile centers in the overbarrier interval $-5 \lesssim vt \lesssim 5$ a.u. Nevertheless the impact velocity is now larger so that the trajectories perform a half twist less than in the previous case; concretely, the trajectories bounce for the sixth time on the (projectile) right exterior potential wall too late, at $vt \gtrsim 4$ a.u., to be able to jump over the internuclear barrier later on (at the lower $E = 0.147$ keV, the trajectories bounced for the sixth time on the right wall earlier, around $vt \lesssim 4$ a.u., and were accordingly able to hop on the target for $vt \gtrsim 4$ a.u.).

Increasing further the impact velocity makes the overbarrier time interval shorter, according to $-5/v \lesssim t \lesssim 5/v$ a.u., and

the number of trajectories' oscillations between the target and projectile centers is consequently reduced. In Fig. 3(c) which illustrates the electron motion for $E = 0.21$ keV, we observe that the trajectories are effectively delayed with respect to those of Fig. 3(b) on a fixed scaled time interval, finally leading to a minimum capture probability $P_C^{\rm clas} \sim 0$. Within one oscillation of the capture probability, as exemplified in Figs. 3(a) and 3(c) by $E = 0.147$ keV and $E = 0.21$ keV, respectively, we note that the trajectories perform one oscillation less between the nuclear centers in the overbarrier region. This leads to a particularly simple and intuitive explanation for the oscillatory behavior of the capture (and corresponding elastic) probabilities: it stems from the dependence of the overbarrier time interval on the impact velocity, $-R_{\rm ob}/v < t < R_{\rm ob}/v$, which determines the number of allowed electron transitions between the nuclear centers before final localization.

One may legitimately cast doubt on the soundness of this classical picture which is apparently difficult to link with Eq. (11). We therefore display in Figs. 3(d)– 3(f) the temporal evolution of the quantum-mechanical electron density $|\Psi(x,t)|^2$, as a function of the scaled time vt and for the same impact energies as in the classical graphs [Figs. 3(a)–3(c)]. A close classical-quantum correspondence shows up as one compares the classical pictures [Figs. 3(a)–3(c)] with their quantum counterparts [Figs. 3(d)–3(f)]. In fact, the accumulative phases $e^{-i\int^t E_k(t')dt'}$ which enter the expansion (3) of Ψ and subsequently lead to Eq. (11) contribute to the description of a classical electron that oscillates between the target and projectile centers in the near collisional region. The number of oscillations is monitored by the dependence of the phases on v, $e^{-i\int^t E_k(t')dt'} = e^{-\frac{i}{v}\int^R E_k(R')dR'}$, with $R = vt$. In the following section, we further prove that Bohmian quantum trajectories validate the classical swapping of the electron between the nuclear centers.

We now turn our attention to the origin of the above-mentioned weak dephasing of the classical and quantal capture probabilities. While back and forth transition hops are restricted to the overbarrier region in the classical framework, some underbarrier transitions are quantum mechanically allowed for $R > R_{\rm ob}$. In the incoming phase of the collision, such additional transitions occur for $vt \gtrsim -6$ a.u., just before overbarrier hopping is allowed [see Figs. 3(d)–3(f)]. The quantum electron dynamics thus occur in advance of their microcanonical counterparts, yielding the weak dephasing of the corresponding final probabilities. The dephasing vanishes as v increases because the delay Δt between under- and overbarrier transitions scales as $\Delta t = \Delta R/v$, with $\Delta R \sim 2$ a.u. We have investigated how the use of improved initial conditions (16), beyond the microcanonical framework (15), allows one to remedy the classical-quantal shift. The truncated Wigner distribution (16) indeed includes electron trajectories with energies $\epsilon^{(T)}$ greater than $\epsilon_1^{(T)}$ and these trajectories are expected to mimic classically the underbarrier transitions [28]. The capture probability obtained by means of the CTMC calculations using $\varrho_{Wt}(x,p)$ is reported in Fig. 2. It is clear that $\varrho_{Wt}(x,p)$ makes the agreement of the quantum and classical descriptions of electron motion worse: the classical-quantal shift is increased and the amplitude of the classical probability oscillations is significantly reduced at low E. These features indicate an improper description of primary tunnel transitions and a subsequent jumbling of the electron oscillations which monitor the shape of the capture probability as a function of E. In practice, we have observed that some trajectories, with energies $\epsilon^{(T)}$ exceeding the internuclear barrier, do hop on the projectile for $vt \gtrsim -6$ a.u., but other ones, with smaller $\epsilon^{(T)}$, remain blocked in the target potential; this picture is not a faithful representation of the quantum tunnel process which occurs in the same vt range and where the electron density moves as a whole from the target to the projectile [see Figs. 3(d)–3(f)]. Later on, swapping between the nuclear centers is allowed for most of the trajectories but the spread of the electron velocity distribution, inherent in $\varrho_{Wt}(x,p)$, impedes those trajectories to evolve as a whole at low E. The dispersed trajectories consequently contribute more equally to the capture and elastic scatterings than in the microcanonical and quantum frameworks. For $E > 1$ keV, the contribution of underbarrier transitions decreases and the effect of dispersion on trajectories does not have time to operate significantly; the capture probability obtained by means of Wigner-CTMC calculations then agrees with its microcanonical analog.

2. *Three-dimensional calculations*

The close-coupling calculations are based on an eight-term CTF-corrected molecular expansion that includes all the OEDMs correlated with $H^+ + H(n)$ and $H(n) + H^+$ up $n = 2$. The CTMC calculations employ $N = 30\,000$ trajectories in a microcanonical framework. To compare the results of these calculations with the previous 1D ones, we set $b = 10^{-3}$ a.u.

In Fig. 4, we report the total capture probability resulting from the close-coupling calculations as a function of E lying in the range $0.05 \leqslant E \leqslant 1$ keV. As before, the computed probability coincides with the expression (11) associated with the minimal two-state expansion without translation factor. The striking difference which appears with respect to the previous 1D simulations is the failure of the CTMC calculations to reproduce the oscillatory behavior of the capture probability, $P_C^{\rm clas} \sim 0.5$ in all the low-impact velocity

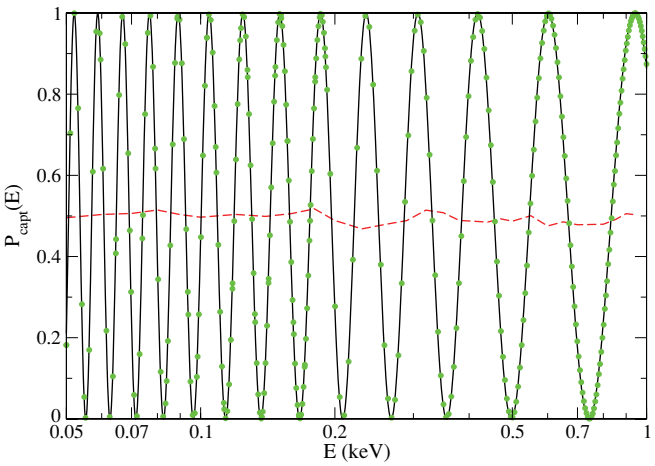

FIG. 4. (Color online) Total capture probability in 3D $H^+ + H(n = 1)$ collisions as a function of the impact energy E: large-scale molecular calculations (—); expected results (green •) from the two-state expansion (11); and CTMC calculations (red – –).

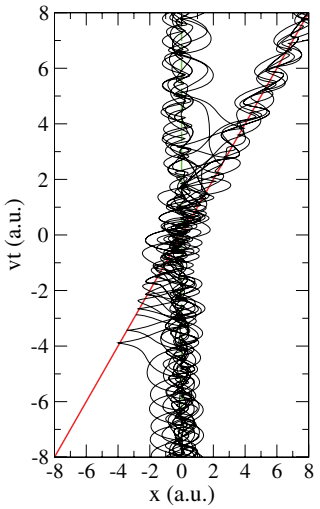

FIG. 5. (Color online) Temporal evolution of the longitudinal coordinate $x_j(t)$ of randomly sorted CTMC electron trajectories in three-dimensional $H^+ + H(n = 1)$ collisions with $E = 0.6$ keV and $b \sim 0$. The electron trajectories (black thin lines) are displayed as functions of the scaled time vt. The target (dashed green line) remains located at $x = 0$ for all t and the projectile trajectory $x(t) = vt$ is drawn with a thick (red) line.

ranges. The small deviations of P_C^{clas} around 0.5 are due to statistical uncertainties and must not be related to genuine collisional effects.

To trace back the root of the failure of the 3D classical treatment, we proceed as in Fig. 3 and display in Fig. 5, for $E = 0.6$ keV, the evolution of the longitudinal cooordinate $x_j(t)$ ($\hat{\mathbf{x}} = \hat{\mathbf{v}}$) of randomly selected CTMC trajectories as a function of the scaled time vt. We observe that the trajectories behave in the longitudinal direction similarly as they evolve in the 1D simulations: they remain blocked in the target potential wall up to $vt \sim -5$ a.u. and then begin to oscillate between the target and projectile centers in the overbarrier region. Nevertheless the trajectories evolve out of phase so that half of them finally follow the target nucleus while the remaining ones are captured. The dephasing of the trajectories exists since their entrance in the overbarrier region as a result of the dispersion induced by the transverse degrees of freedom y and z. In practice, the transverse momenta $p_y(t)$ and $p_z(t)$ strongly influence the moments where the classical electrons bounce on the exterior walls of the total potential in the longitudinal direction. Therefore, and contrary to what has been observed in the 1D simulations of Fig. 3, the 3D CTMC trajectories do not evolve as a whole in the longitudinal direction as it is required to reproduce the oscillatory behavior of the capture probability.

We are thus led to examine the behavior of Bohmian trajectories to understand how and why the probability oscillations arise in the 3D quantum framework. Among all the quantum trajectories that belong to the initial state at $t = t_{\text{in}}$, we decided to follow the motion of some prototypical ones, initially located in the (x,z) collisional plane as shown schematically in Fig. 6(a); some of them lie in the internuclear direction $z = 0$ (as in Fig. 3) while the remaining ones are located in symmetric transverse directions given by $z = -2$ a.u. and $z = 2$ a.u.,

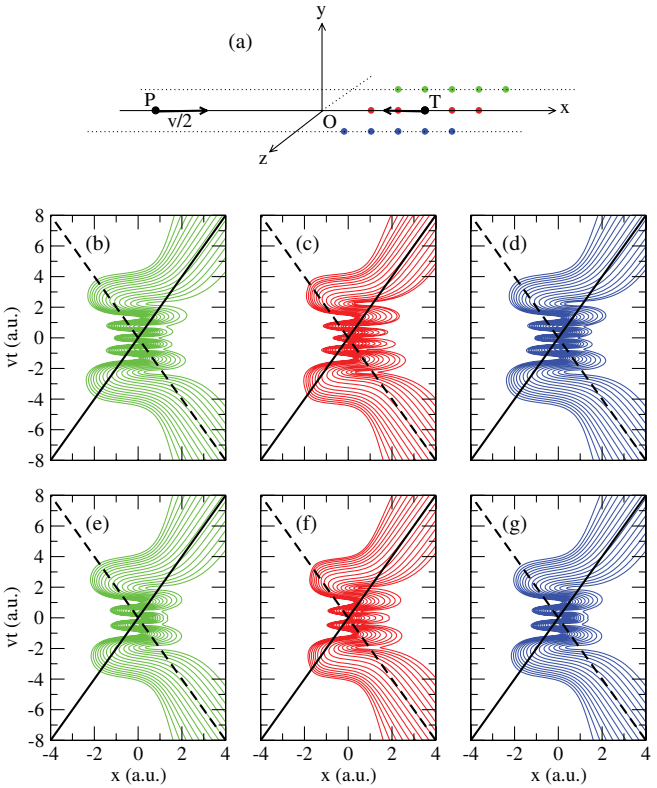

FIG. 6. (Color online) Temporal evolution of Bohmian trajectories in 3D head-on $H^+ + H(1s)$ collisions. Three subsets of Bohmian trajectories are selected as shown schematically in (a): a first subset includes trajectories initially located around the target nucleus in the internuclear direction $z = 0$ (red points, on middle line); the second and third subsets correspond to trajectories located in the transverse directions $z = -2$ a.u. (green points, on top line) and $z = 2$ a.u. (blue points, on bottom line). The origin of electron coordinates is chosen at the midpoint of the H_2^+ system so that the target (T) and projectile (P) travel with respective velocities $-v/2$ and $v/2$ in the x direction; the trajectories of T and P are represented by the dashed and plain thick lines, respectively, in (b–g). In (b–d), we display the evolution of the longitudinal coordinate $x_j(t)$ of the trajectories as a function of the scaled time vt for the impact energy $E = 0.6$ keV; (b), (c), and (d), respectively, refer to the trajectories initially located on the axis $z = -2$ a.u., $z = 0$ a.u., and $z = 2$ a.u. In (e–g), we display the same as in (b–d) but for $E = 0.94$ keV.

respectively. The origin of electron coordinates is $p = 1/2$ so that the target and the projectile move with respective velocities $-v/2$ and $v/2$ along the x direction. Initially (at $t = t_{\text{in}}$), all the Bohmian trajectories evolve with $\mathbf{v}_j(t) \sim -\mathbf{v}/2$. We then compare in Figs. 6(b)–6(g) the evolution of the longitudinal motion $x_j(t)$ of the selected quantum trajectories at $E = 0.6$ [Figs. 6(b)–6(d)] and $E = 0.94$ keV [Figs. 6(e)–6(g)] that coincide with two consecutive locations of probability maxima (see Fig. 4).

Let's first consider the quantum trajectories initially located along the x axis [Fig. 6(c)]. The similarity of their behavior with that of the classical trajectories of Fig. 3(b) is striking. As soon as it enters into the overbarrier region, the Bohmian flow exhibits the back and forth motion between the target and projectile centers. This whole motion is dictated by the outer trajectories with significant weights ρ_j that consecutively

bounce on the outer walls of the molecular potential. As the trajectories cannot cross, since $\mathbf{v}_j = \nabla S|_j$ is single valued at a given $\mathbf{r}_j$, the inner trajectories do not really bounce on the external potential walls but rather follow the motion constrained by the outer trajectories. Finally all the quantum trajectories localize on the projectile to yield $P_C = 1$.

Because of the azimuthal symmetry around the x axis, all the quantum trajectories of Fig. 6(c) have transverse velocity components which remain equal to 0 throughout the collision. This is not the case for the trajectories of Figs. 6(b) and 6(d) which were initially located in the transverse directions $z = -2$ a.u. and 2 a.u., respectively. These trajectories present $v_y = 0$ to obey symmetry with respect to the collisional (x,z) plane, but $v_z \neq 0$. In practice, v_z remains quite small in the course of the collision, because of the noncrossing rule mentioned above, and the transverse motions of left $(z < 0)$ and right $(z > 0)$ trajectories are symmetric with respect to the x axis. Both sets of trajectories evolve identically in the longitudinal direction and display, like the $z = 0$ trajectories, the classical back and forth motion in the overbarrier region which is at the root of the maximal capture probability $P_C = 1$.

As we consider in Figs. 6(e)–6(g) $E = 0.94$ keV, which consists of the impact energy leading to the next $P_C = 1$ condition after $E = 0.6$ keV, we observe that the Bohmian trajectories depict the same classical behavior as in the previous case, but perform one oscillation less between the nuclear centers in the overbarrier region. The origin of probability oscillations drawn from our 1D CTMC study is thus clearly ascertained in the quantum framework: it stems from the dependence of the overbarrier time interval on the impact velocity, $-R_{\rm ob}/v \leqslant t \leqslant R_{\rm ob}/v$, which determines the number of allowed electron transitions between the nuclear centers before final localization.

In the light of Fig. 6, we understand that what is clearly failing in the 3D statistical description is the reproduction of trajectories' entanglement. CTMC is succeeding in describing the (quantumlike) initial average conditions on the transverse electron velocity components, $\langle v_y(\mathbf{r})\rangle_\varrho = \langle v_z(\mathbf{r})\rangle_\varrho = 0$, by means of a large ensemble of noninteracting trajectories with significant velocity spread [46]. However, large tranverse components, compared to v, put the independent electron trajectories out of phase in the longitudinal direction in which no overall motion can then show up (see Fig. 5). In this respect, the introduction of an artifical viscosity term [51] in the classical equations of motion should remedy this, entangling the CTMC trajectories. Such an entanglement must not be interpreted as a major quantum effect. We indeed know that quantum effects generally induce the apparition of nodes or deep minima in the total electron wave function [53]; in the present case, we have explicitly verified by means of our close-coupling calculations that the total Ψ is weakly structured, which is a sign of both weak quantum effects and related dominance of classical behavior, as corroborated by the Bohmian trajectories of Fig. 6.

B. $He^{2+} + H(n = 1)$

We now consider 1D $He^{2+} + H(n = 1)$ collisions as a prototype of multicharged ion-atom collisions. The He^+ states are obtained by diagonalization of the atomic Hamiltonian in a

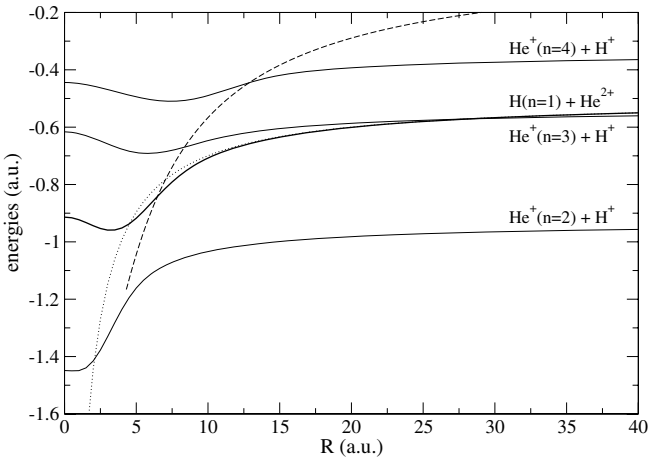

FIG. 7. Correlation diagram of the 1D $He^{2+} + H$ system: the plain lines correspond to the molecular energies $E_n(R)$ as functions of the internuclear distance R; the dotted line refers to the energy of the electron in its initial target state perturbed by the projectile located at distance R; and the dashed line illustrates the height of the internuclear potential barrier as a function of R.

$\{\cos(kx), \sin(kx)\}$ basis defined by $x_{\rm max}^{(P)} = 50$ a.u. and $k_{\rm max}^{(P)} = 6$ a.u., yielding 16 bound and 174 discretized continuum states. The molecular states $\chi_m(x,R)$ are obtained similarly by diagonalizing H (2) in a basis characterized by $x_{\rm max} = 150$ a.u. and $k_{\rm max} = 6$ a.u. The $\{\chi_m(x,R)\}$ basis includes 36 bound and 536 continuum wave functions. The classical CTMC calculations employ $N = 30\,000$ noninteracting trajectories.

We display in Fig. 7, as functions of R, the energies of the molecular states associated with the entrance state and main capture channels. We also include in this figure the energy $\epsilon_1^{(T)} - 2/\sqrt{R^2 + 1/2}$ of the electron in its initial state perturbed by the projectile located at distance R, as well as the height $V_{\rm max}(R)$ of the internuclear total potential. The comparison of these two quantities shows that overbarrier transitions between the target and the projectile are allowed for $R \lesssim 7$ a.u.

The total capture probability obtained by means of the molecular calculations is drawn in Fig. 8 as a function of the impact energy E with $1 \leqslant E \leqslant 200$ keV/amu. $P_C(E)$ presents an oscillatory shape with an amplitude less than 1. In the close-coupling framework, the origin of the (Stueckelberg) oscillations can be traced back to the phase differences which appear in the set of differential equations (4) defining the expansion coefficients.

The classical probability resulting from microcanonical CTMC calculations is included in Fig. 8. As for $H^+ + H$ collisions, the oscillatory behavior of the probability is fairly reproduced. To elicit the origin of the classical oscillations, we draw in Fig. 9 the temporal evolution of randomly sorted CTMC trajectories for $E = 1.21$, 1.66, and 3 keV/amu [within one oscillation of $P_C(E)$, see Fig. 8]. The scenario that applied for the previous homonuclear system is clearly repeated in the present case: the trajectories remain trapped in the target potential well until they reach the overbarrier region where they start to bounce off the outer walls of the molecular

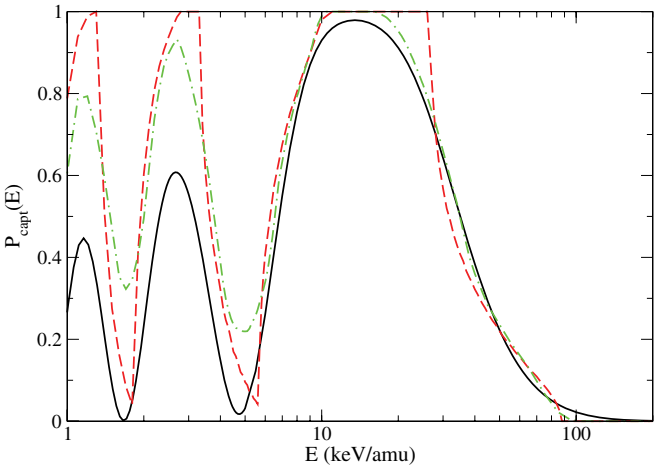

FIG. 8. (Color online) Total capture probability in 1D $He^{2+} + H(n = 1)$ collisions as a function of the impact energy E: large-scale molecular calculations (—); CTMC calculations with microcanonical (red dashed line) and truncated Wigner (green dot-dashed line) initial conditions.

potential; for the selected impact energies of Fig. 9, the initial dispersion of the trajectories has no consequence on the subsequent global electron flow which finally localizes around one nuclear center according to the number of bounces allowed in the overbarrier time interval that shrinks as $-R_c/v < t < R_c/v$ with increasing v. For impact energies in between those of Fig. 9, the initial phase of the electron plays a role since the trajectories arrive at the exit of the overbarrier region with a delay that impedes the last trajectories to hop on the nuclear center where the first (prompter) electrons have localized; the final capture probability is consequently neither 0 nor 1.

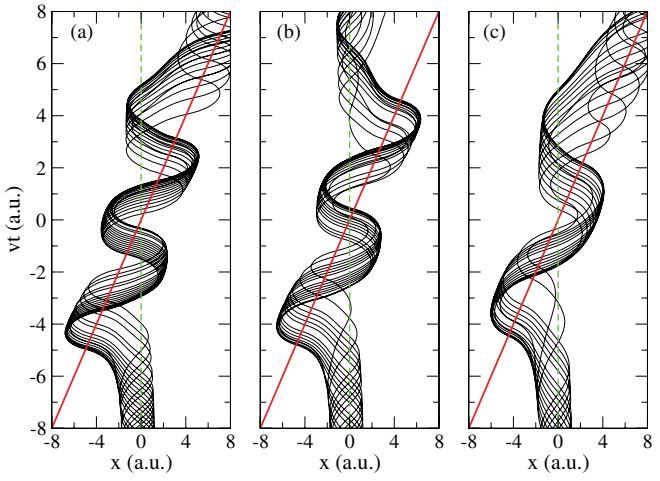

FIG. 9. (Color online) Temporal evolution $x_j(t)$ of randomly sorted CTMC electron trajectories in 1D $He^{2+} + H(n = 1)$ collisions. The trajectories (black thin lines) are displayed as functions of the scaled time vt for the impact energies $E = 1.21$ (a), 1.66 (b), and 3 (c) keV/amu. The target (dashed green line) remains located at $x = 0$ for all t and the projectile trajectory $x(t) = vt$ is drawn with a thick (red) line.

For $E < 10$ keV/amu, the amplitude of the classical probability is overestimated with respect to its quantum analog. This is due to the lack of underbarrier transitions (occuring for $R > R_c$) in the classical microcanonical framework. Therefore we have performed Wigner-CTMC calculations and the results are included in Fig. 8. The magnitude of the probability maxima is suitably reduced for $E < 10$ keV/amu, even though it does not decrease enough to match the quantum value, but the minima are no more 0 as they should be (and were in the microcanonical calculations). This reiterates the fact that the improvement of initial CTMC conditions, beyond the microcanonical framework, does not provide a faithful enough representation of tunnel transitions in low-energy atomic collisions.

IV. CONCLUSIONS

In this paper, we have considered the behavior of the total charge-exchange probability in low-energy ion-atom collisions. It is well known that this probability exhibits oscillations either as a function of b for fixed v or as a function of v for fixed b. These oscillations are usually interpreted as signatures of quantum (interference) effects because they result, in the close-coupling formulation of the collision dynamics, from v- and b-dependent phase terms involving energy differences between the capture and elastic scattering channels.

We have performed molecular close-coupling and classical CTMC calculations of the charge-exchange probabilities in low-energy $H^+ + H(n = 1)$ and $He^{2+} + H(n = 1)$ collisions. In a first step, we have used a reduced (1D) dimensionality and have studied the dependence of the probabilities on the impact energy E for $b = 0$. We have found that the oscillatory behavior of the probabilities is fairly represented by means of the microcanonical CTMC method, even in the case of $H^+ + H(n = 1)$ where the main capture and elastic scattering channels are symmetrically resonant. The temporal evolution of the classical trajectories has thus allowed us to propose a classical interpretation of the oscillations, as an alternative to the usual quantum explanation: the trajectories remain trapped in the target potential well until they reach the overbarrier region $R < R_c$ where they start to bounce off the outer walls of the molecular potential; the final localization of the electron then depends on the number of bounces allowed within the overbarrier time interval that shrinks according to $-R_c/v < t < R_c/v$ as v increases. This finding is consistent with previous works (see, e.g., Refs. [36,37]) which already linked classical swapping of the electron between the colliding nuclear centers to quantum-interference patterns.

We have also performed 3D calculations for the same systems. The probability oscillations did not show up in the 3D CTMC simulations because of the additional tranverse degrees of freedom which induce a strong dephasing of the trajectories in the longitudinal (internuclear) direction throughout the collision. The tranverse components of the electron momentum tend to distribute the noninteracting CTMC trajectories more uniformly between the nuclear centers at the exit of the overbarrier region. In a quantum description, these transverse

components do not blur the whole electron flow because of the entanglement of the trajectories; 3D Bohmian trajectories evolve as a whole in the longitudinal direction, similarly to what happens in the 1D CTMC framework. Even if this shows that 3D CTMC calculations cannot substitute exact quantum-mechanical descriptions, the fact remains that the probability oscillations can be classically understood as in 1D model systems.

[1] R. C. Isler, Plasma Phys. Controlled Fusion **36**, 171 (1994).
[2] T. E. Cravens, Science **296**, 1042 (2002).
[3] H. Luna *et al.*, Phys. Rev. A **75**, 042711 (2007).
[4] B. H. Bransden and M. H. C. McDowell, *Charge Exchange and the Theory of Ion-Atom Collisions* (Clarendon, Oxford, 1992).
[5] D. Belkic *et al.*, At. Data Nucl. Data Tables **51**, 59 (1992).
[6] E. A. Solov'ev, J. Phys. B **38**, R153 (2005).
[7] C. Harel, H. Jouin, and B. Pons, At. Data Nucl. Data Tables **68**, 279 (1998).
[8] W. Fritsch and C. D. Lin, Phys. Rep. **202**, 1 (1991).
[9] L. F. Errea *et al.*, J. Phys. B **31**, 3199 (1998).
[10] N. Toshima, Phys. Rev. A **59**, 1981 (1999).
[11] T. Kirchner *et al.*, Rec. Res. Dev. Phys. **5**, 433 (2004).
[12] H. J. Lüdde, T. Spranger, M. Horbatsch, and T. Kirchner, Phys. Rev. A **80**, 060702 (2009).
[13] T. Minami *et al.*, J. Phys. B **40**, 3629 (2007).
[14] T.-G. Lee, S. Y. Ovchinnikov, J. Sternberg, V. Chupryna, D. R. Schultz, and J. H. Macek, Phys. Rev. A **76**, 050701 (2007).
[15] H. Knudsen, H. K. Haugen, and P. Hvelplund, Phys. Rev. A **23**, 597 (1981).
[16] R. Abrines and I. C. Percival, Proc. Phys. Soc. London **88**, 861 (1966).
[17] R. E. Olson and A. Salop, Phys. Rev. A **16**, 531 (1977).
[18] C. O. Reinhold and C. A. Falcon, J. Phys. B **21**, 2473 (1988).
[19] C. Illescas and A. Riera, Phys. Rev. A **60**, 4546 (1999).
[20] D. J. W. Hardie and R. E. Olson, J. Phys. B **16**, 1983 (1983).
[21] D. Eichenauer, N. Grun, and W. Scheid, J. Phys. B **14**, 3929 (1981).
[22] J. S. Cohen, J. Phys. B **18**, 1759 (1985).
[23] D. R. Schultz, P. C. Stancil, and M. J. Rakovic, J. Phys. B **34**, 2739 (2001).
[24] L. F. Errea, C. Illescas, L. Mendez, B. Pons, A. Riera, and J. Suarez, Phys. Rev. A **70**, 052713 (2004).
[25] P. Botheron and B. Pons, Phys. Rev. A **80**, 023402 (2009).
[26] E. P. Wigner, Phys. Rev. **40**, 749 (1932).
[27] H. W. Lee, Phys. Rep. **259**, 147 (1995).
[28] E. A. Solov'ev, JETP **76**, 934 (1993).
[29] A. Wang *et al.*, Phys. Chem. Chem. Phys. **11**, 1588 (2009).
[30] L. F. Errea *et al.*, J. Phys. B **37**, 4323 (2004).
[31] L. F. Errea *et al.*, Plasma Phys. Controlled Fusion **48**, 1585 (2006).
[32] G. J. Lockwood and E. Everhart, Phys. Rev. **125**, 567 (1962).
[33] L. F. Errea *et al.*, J. Phys. B **31**, 3527 (1998).
[34] E. C. G. Stueckelberg, Helv. Phys. Acta **5**, 369 (1932).
[35] K. B. MacAdam, J. C. Day, J. C. Aguilar, D. M. Homan, A. D. MacKellar, and M. J. Cavagnero, Phys. Rev. Lett. **75**, 1723 (1995).
[36] D. R. Schultz, C. O. Reinhold, and P. S. Krstić, Phys. Rev. Lett. **78**, 2720 (1997).
[37] P. S. Krstić, C. O. Reinhold, and D. R. Schultz, J. Phys. B **31**, L155 (1998).
[38] R. K. Janev, J. Pop-Jordanov, and E. A. Solov'ev, J. Phys. B **30**, L353 (1997).
[39] A.-T. Le, C. D. Lin, L. F. Errea, L. Mendez, A. Riera, and B. Pons, Phys. Rev. A **69**, 062703 (2004).
[40] W. H. Press *et al.*, *Numerical Recipes* (Cambridge University Press, Cambridge, UK, 1986).
[41] L. F. Errea *et al.*, J. Chem. Phys. **121**, 1663 (2004).
[42] A. Macias and A. Riera, Phys. Rep. **81**, 299 (1982).
[43] L. F. Errea *et al.*, J. Phys. B **27**, 3603 (1994).
[44] L. F. Errea, C. Harel, H. Jouin, L. Mendez, B. Pons, A. Riera, and I. Sevila, Phys. Rev. A **65**, 022711 (2002).
[45] B. Pons, Phys. Rev. Lett. **84**, 4569 (2000); Phys. Rev. A **63**, 012704 (2000).
[46] C. Illescas, B. Pons, and A. Riera, Phys. Rev. A **63**, 062722 (2001).
[47] A. Kolakowska, M. S. Pindzola, F. Robicheaux, D. R. Schultz, and J. C. Wells, Phys. Rev. A **58**, 2872 (1998).
[48] M. Chassid and M. Horbatsch, J. Phys. B **31**, 515 (1998).
[49] D. Bohm, Phys. Rev. **85**, 166 (1952); **85**, 180 (1952).
[50] V. E. Madelung, Z. Phys. **40**, 322 (1926).
[51] R. E. Wyatt, *Quantum Dynamics with Trajectories* (Springer, Berlin, 2005).
[52] G. Terlecki, N. Grun, and W. Scheid, J. Phys. B **17**, 3719 (1984).
[53] P. Botheron and B. Pons, Phys. Rev. A **82**, 021404(R) (2010).